ARTICLE

Transition from Escaped to Decomposed Nematic Defects, and *vice versa*

Received 00th January 20xx,
Accepted 00th January 20xx

DOI: 10.1039/x0xx00000x

Adam L. Susser[a], Saša Harkai[b], Samo Kralj[b], and Charles Rosenblatt[a]

An escaped radial director profile in a nematic liquid crystal cell can be transformed into a pair of strength m = +½ surface defects (and their associated disclination lines) at a threshold electric field. Analogously, a half-integer defect pair can be transformed at a threshold electric field into a director profile that escapes into the third dimension. These transitions were demonstrated experimentally and numerically, and are discussed in terms of topologically discontinuous and continuous pathways that connect the two states. Additionally, we note that the pair of disclination lines associated with the m = +1/2 surface defects were observed to co-rotate around a common point for a sufficiently large electric field at a sufficiently low frequency.

1 Introduction

Topological defects (TDs) occur throughout nature, from the nanoscopic to the cosmological level[1-5]. Because of their large optical and mechanical anisotropies, liquid crystals (LCs) have become an ideal playground for visualizing TDs and studying their physical behaviour[6-10]. In particular, LCs have been used to understand the energies and transformations associated with TDs[9,11].

The energy cost of nematic topological defects of total strength m = +1 at each of two opposing substrates, and the disclination line connecting them, may be relaxed via various mechanisms. These include i) melting of the core, ii) biaxial order reconstruction[12,13], iii) director escape along an axis perpendicular to the surface (Fig. 1a)[14-16], and iv) decomposition of an integer defect into a pair of half-integer surface defects (Fig. 1b)[11,17,18]. In the latter case two disclination lines connect the two m = +½ surface defects with the opposing substrate – this tends to occur in thinner cells[9,11]. (Alternatively, an arched disclination connects the two m = +½ defects with each other at the same surface[10,19] – this tends to occur in thicker cells.) Mechanisms iii and iv are observed most commonly and have garnered the most attention. Recent studies have focused on sample thickness and the operative mechanisms that reduce energy cost.[9,11] Observations have shown that integer defects or escaped radial (ER) configurations can be converted into a pair of half-integer defects, and *vice versa*, by heating the entire liquid crystal into the isotropic phase followed by recooling into the nematic phase[9]. But is there another way to achieve this interconversion?

Imagine an ER director configuration composed of a negative dielectric anisotropy ($\Delta\varepsilon < 0$) liquid crystal connecting top and bottom substrates (Fig. 1a). Here the director field has positive uniaxial symmetry. An ac electric field E is applied perpendicular to the substrates along the z-axis, which has the effect of pushing the director field into the xy-plane. For one pathway the defect core must melt so as to convert the director field in the core from positive to negative uniaxial symmetry, which is a necessary step in transitioning to an m = +1 defect that subsequently decomposes into a pair of m = +½ defects. This melting would take place at a specific threshold electric field E_{th}. The occurrence of melting suggests that the two end states in this process, *viz.*, an ER configuration and a pair of decomposed half-integer defects, would be topologically distinct, with a discontinuous pathway between the two. Note that the reverse transition also can be driven by an electric field for a liquid crystal with a positive dielectric anisotropy ($\Delta\varepsilon > 0$).

An alternative pathway consists of an ER structure in which there is strong planar anchoring at the bottom surface that gives rise to a proper m = +1 surface defect. Even at zero field this integer defect would split into two m = +½ *surface* defects,

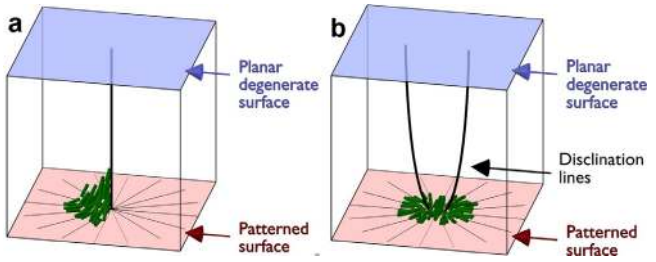

Fig. 1 Cartoons showing a master surface that has been patterned with an m = +1 defect and an opposing substrate treated for planar degenerate alignment. a) Escaped radial director configuration, and b) Splitting of the m = +1 pattern into two daughter m = +½ surface defects, with disclination lines reaching the top planar degenerate opposing surface.

[a] Department of Physics, Case Western Reserve University, Cleveland, Ohio 44106 USA
[b] Department of Physics, Faculty of Natural Sciences and Mathematics, University of Maribor, Koroška cesta 160, SI-2000 Maribor, Slovenia and Jožef Stefan Institute, P.O. Box 3000, SI-1000 Ljubljana, Slovenia

Electronic Supplementary Information (ESI) available: Videos of the ER to split and the split to ER transitions. See DOI: 10.1039/x0xx00000x

causing the defect to appear elongated under a microscope – or even as two discrete half-integer defects. These half-integer defects *at the same surface* are connected by a "charged" boojum disclination loop[10,19] – actually an arch that becomes elongated along the arch's axis as one transits along the *z*-axis into the cell. The loop has a strength of m = +½, such that the director field around the loop is three-dimensional[10]. However, with increasing electric field the director field is pushed more strongly into the xy-plane, thereby driving the boojum loop upward, as shown recently by Ferris, *et al*.[10] At a critical electric field the loop would reach the top surface and split, thereby connecting each of the m = +½ defects at the top substrate with the bottom substrate by means of a disclination line, similar to that shown in Fig. 1b. This transition pathway is continuous, which suggests that the two terminal configurations need not be topologically distinct.

In this paper we report on experiments in which an electric field is used to convert an ER configuration into a pair of m = +½ surface defects and their related disclination lines, and *vice versa*. The ER to m = +½ defect pair transition is accomplished by using a negative dielectric anisotropy liquid crystal, in which the electric field drives the director into the xy-plane; the opposite transition involves a positive anisotropy liquid crystal in which the electric field drives the director toward an ER configuration, *i.e.*, toward the z-axis. For the ER to split transition, optical microscope observations – both bright field and polarized optical microscopy – show only a tightening of the defect core(s) as the electric field is increased, with no significant change in the director field outside the defect core(s). But at a sufficiently large field – this is the threshold field E_{th} – a transition occurs from ER to decomposed half-integer defects (or *vice versa*, as appropriate). On removal of the electric field the new director configuration remains stable.

2 Experimental

Two cells were constructed from semi-transparent indium-tin-oxide (ITO) coated glass slides, with the ITO used as electrodes. One slide was spin-coated with the polymer polyvinyl alcohol (PVA, M_w = 31000 – 50000) and baked at 120°C for 120 min. The PVA then was scribed by an atomic force microscope with a patterned 3 x 3 array of alternating m = +1 and -1 defects using the method described in Ref. 17, with scribed line spacing ~ 100 nm; this is the bottom "master" surface. The opposing top substrate was spin-coated with a thin layer of Glymo ((3-Glycidyloxypropyl)trimethoxysilane), which was diluted to a concentration of 0.5 wt-% in isopropyl alcohol (89.5 wt-%) and water (10 wt-%). The substrate was spun for 30 s at 2200 rpm, and then baked at 170°C for 60 min. The slides for each cell were placed together, separated by Mylar spacers, and cemented. The thicknesses h of the various cells were in the range 6.4-8.4 μm as determined by optical interferometry. This thickness has been shown to produce a mixture of ER configurations and split defects, although *a priori* a mixed set of ER and split defects is not guaranteed. Our experiments focused on the m = +1 pattern.

For the initially ER configuration, we used the negative dielectric anisotropy mixture liquid crystal ZLI-4330 (Merck), which has a room temperature nematic phase. Its dielectric anisotropy $\Delta\varepsilon$ = -1.9 and its optical birefringence Δn = 0.15 [manufacturer's specifications] measured at room temperature. The cell of thickness 7.9 < h < 8.4 μm was filled in the isotropic phase by capillary action and then cooled into the nematic phase, with all subsequent measurements performed at room temperature. In order to ensure an ER configuration, even if only split defects appeared on first cooling into the nematic phase, the sample was reheated into the isotropic phase and cooled more rapidly into the nematic phase. The rapid cooling was found to promote the ER configuration at the patterned m = +1 sites.

For the initially split defect experiments, we used the positive dielectric anisotropy liquid crystal pentylcyanobiphenyl (5CB, Merck), having a room temperature dielectric anisotropy $\Delta\varepsilon$ = +11.0 and optical birefringence Δn = 0.18 [manufacturer's specifications]. The cell of thickness 6.4 < h < 7.9 μm was filled with the LC in the isotropic phase and cooled to room temperature. If, by chance, the initial configuration were ER, we found empirically that gentle mechanical agitation of the cell could induce a split m = +½ defect pair, with two quasi-parallel disclination lines running from one substrate to the other.

3 Experimental Results and Discussion

Consider first an initially ER configuration in the negative dielectric anisotropy ZLI-4330 sample. An ac voltage at frequency ν = 1 kHz was applied between the two substrates, and ramped (actually incrementally stepped) up to 243 V at a rate of ~1 V s^{-1}. Bright field images (no polarizers) were recorded for one ramping (see Electronic Supplementary Information video 1). Transmission polarized optical microscopy images were recorded for the

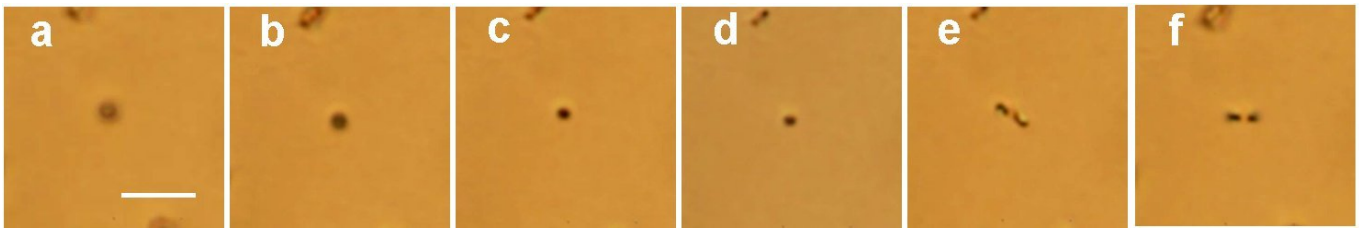

Fig. 2 Progression of ER to split defects at E = a) 0, b) 0.9, c) 2.5, d) 29.6 V μm^{-1}. Then e) 29.6, f) 0 V μm^{-1}. Scale bar corresponds to 15 μm.

subsequent ramping. We observed the following features seen in the bright field images of Fig. 2:

1. The initial defect core at voltage V = 0, i.e., at field E = 0, appeared circularly symmetric for both polarized and bright field measurements. That is, there was no elongation or splitting observed within the limits of resolution (Fig. 2a)
2. With increasing voltage, the defect core became more sharply focused and less washed out – this was especially noticeable in the bright field images (Figs. 2b-2d). The most rapid changes in sharpness occurred at low voltage, but the circular shape (as opposed to size) of the core did not change with voltage up to a threshold voltage V_{th} of 241 V, corresponding to a threshold electric field E_{th} of approximately 29.2 V μm^{-1} (Fig. 2e). We remark that these values were observed to vary by as much as 20% among the patterned defect sites, possibly due to small variations in the local anchoring strength, dust, tiny bubbles, etc. (See discussion following item 8.) We also remark that given the high resistance of the cell (~ 10^{10} Ω), the power dissipation is of order a few microwatts, and thus has negligible effect on the results.
3. At voltages just before reaching V_{th}, the brushes near the core in the polarized microscope images displayed rapid perturbations in shape.
4. Above this threshold voltage the defect decomposed into a pair of half-integer defects over a time scale smaller than 1/f, where f is our video frame rate corresponding to f = 30 frames s^{-1}.
5. The split m = +½ defects were not well-defined spots, but instead appeared to be nearly collinear bowed line segments of length 2 - 3 μm (Fig. 2e). The segment length corresponds to the disclination length projected into the xy-plane.
6. The line segments co-rotated about a common center at a time-varying angular velocity ω that depended on the applied voltage amplitude and frequency. (See Electronic Supplemental Information, video 1.) ω became more rapid as the line segments drew inward and became shorter; ω became slower as the line segments lengthened. This oscillation between shorter and longer segments occurred over a time scale of order 1 s, but was not periodic.
7. The angular rotation frequency ω was found to decrease as the voltage was reduced, reaching ω = 0 at a non-zero voltage. Here the co-rotation of the defects had ceased.
8. The split m = +½ defects remained present with decreasing V, even down to V = 0 (Fig. 2f).

That the initial defect core did *not* give the appearance of a pair of half-integer surface defects with a disclination loop suggests that the transition pathway from ER to a pair of split defects is discontinuous. (See discussion in Section 1.) This is supported by the absence of any visible change in the circular shape of the core region for $V < V_{th}$, *i.e.*, there was no indication of a boojum disclination loop at V = 0 that would alter in appearance as it is pushed toward the opposing substrate by the increasing electric field. These features would suggest that the alternative continuous pathway described in section 1 is *not* the operative mechanism, at least experimentally. Rather, the likely scenario is the first pathway in which the defect core must melt to create negative uniaxial symmetry and a proper m = +1 defect before splitting can occur. This would occur rapidly in the region around $V_{th,}$ corresponding to Figs. 2d and 2e. Why might this be the case? The continuous pathway mechanism requires (near) planar alignment of the director at the master surface in order to accommodate topologically protected surface defects of strength m = +½. If the polar anchoring strength were *not* sufficient to enforce this planar condition, the initial V = 0 configuration at the substrate would be ER with no disclination loop present. Here the defect core would appear cylindrically symmetric and washed out in bright field images due to the spatial variation of the optical retardation α, which corresponds to the phase difference between the ordinary and extraordinary components of the optical polarization: $\alpha = \int k\Delta n dz$, where k is the wavevector of light (=2π/λ, where λ is the wavelength of light) and $\Delta n(r)$ is the effective birefringence due to the out-of-plane director component that varies with position r from the defect core. This was as observed in Figs. 2a-c. To be sure, very strong anchoring would facilitate the planar alignment at the surface that is necessary for the half-integer defects. Thus, stronger anchoring could provide the appropriate continuous pathway, but for our case, at least, the experimental results strongly suggest weaker anchoring and a discontinuous pathway with a change in topology.

The bowed line segments represent a projection of the "charged" disclination lines that run from the m = +½ defects at the patterned (master) surface to their counterpart defects at the opposing surface. As shown by Murray, et al[9], the tendency for the pair of charged disclination lines to mutually repel causes the disclinations to tilt with respect to the surface normal, as they are pinned more strongly at the patterned master surface than at the opposing surface (Fig. 1b). This is the phenomenon seen in Fig. 2e, although the cause of the bowed shape is not immediately apparent.

As noted in bulleted item 6 of Section 3, the split defects underwent rotational motion around a common point. This is an example of what might be described as active behaviour in a nematic in which the co-rotating disclination motion is driven by a possible symmetry-breaking electric field[20] and associated current, a topic for which the literature is very sparse[21,22]. Alternatively, the observed co-rotation may be due to a Lehmann-like effect[23]. This effect could be triggered by a current of free ions present in the sample in the ion conductive regime. Relatively strong elastic distortions localised at cores of defects might produce a sufficiently strong local polarisation

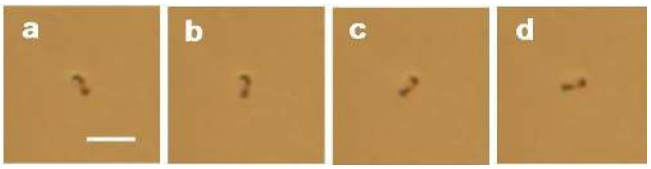

Fig. 3 Co-rotation of defect pair slightly below the threshold field after the ER to split transition occurred. Approximately 33 ms separate successive images. Scale bar corresponds to 15 μm.

due to the LC piezoelectricity. A coupling between the current and defect-generated polarisation thus might generate a torque, resulting in the rotation of defects. Although a full investigation of this phenomenon is beyond the scope of the current work, we present here several experimental observations associated with this phenomenon.

Figure 3 shows a series of frames from the bright field video (Electronic Supplementary Information, video 1) at an applied electric field E = 28.5 V μm^{-1}, which is slightly below the threshold field E_{th} when the field was reduced after the ER to split defect transition had been reached. Here we see the m = +½ defect pair rotating clockwise. Other observations include:

9. When other defect pairs were observed, the rotation sometimes had the opposite sense. The sense of rotation likely is a result of symmetry-breaking surface imperfections.
10. The split defects rotated only above a frequency-dependent critical voltage $V_c(\nu)$ in the h = (8.1 ± 0.3) μm thick cell, where ν is the frequency of the applied voltage (Fig. 4); for $V < V_c(\nu)$ the defects remained fixed.
11. $V_c(\nu)$ appears to be proportional to $\nu^{1/2}$, as witnessed by the linear relationship of V_c^2 vs. ν (Fig. 4). Moreover, after the ER to split transition occurred at $E = E_{th}$, the co-rotation continued even as the field was reduced – until the voltage was reduced below $V_c(\nu)$.
12. The rotation seen in Fig. 3 was highly irregular: The relatively slow rotation was punctuated at irregular intervals of 0.5 to 3 s with much more rapid bursts of rotation, with angular velocities increasing by a factor of 5 to 10 and with the "arms" of the defects drawing inward. (Electronic Supplementary Information, video 1)
13. We have not yet determined if the stable-rotating critical voltage in Fig. 4 corresponds to a critical *field* $E_c = V_c/h$; this is beyond the scope of this work and will be examined in the future.

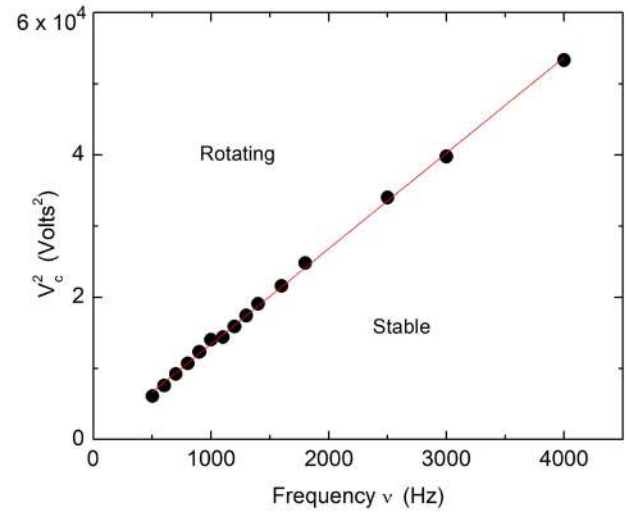

Fig. 4 Critical voltage square vs. frequency ν of applied voltage for the onset of co-rotation of daughter defects in the $\Delta\varepsilon < 0$ liquid crystal. Red line is a two parameter linear least-squares fit to the data. Cell thickness is h = 8.1 μm.

14. The co-rotation occurred only for a negative dielectric anisotropy liquid crystal; for the $\Delta\varepsilon > 0$ liquid crystal 5CB, split m = +½ defect pairs were found to be stable for all voltages and frequencies ν examined.

Reference 21 suggests that non-colinearity of the electric field and the tilted disclination lines play a role in the active behaviour, but this tilt occurs for both positive and negative dielectric anisotropy samples. This leads us to suspect that the opposite signs of the dielectric and conductivity anisotropies for the $\Delta\varepsilon < 0$ liquid crystal ZLI-4330 may play a key role, as can occur in, *e.g.*, a Carr-Helfrich instability[24]. This opposite sign behaviour also is not inconsistent with a Lehmann-type effect, as noted above.

Let us now turn to the transition from a pair of m = +½ surface defects and their associated disclination lines to an escaped radial configuration on application of a sufficiently large electric field (See Electronic Supplementary Information, video 2). An ac voltage at frequency ν = 1 kHz was applied across the $\Delta\varepsilon > 0$ sample of 5CB, and was ramped upward at a rate of ~0.1

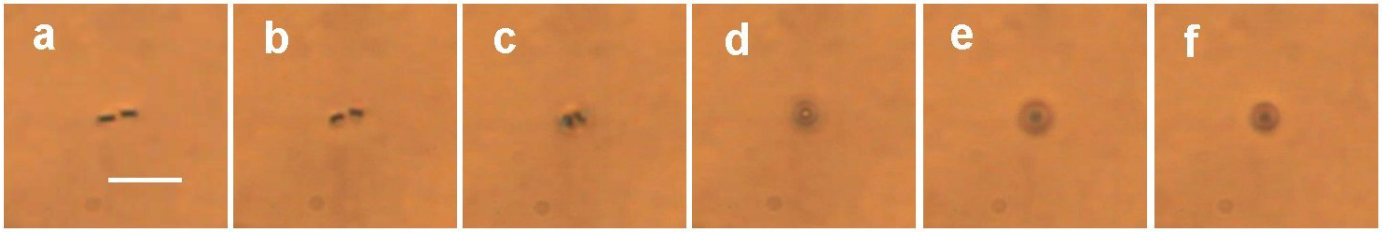

Fig. 5 Progression of m = +½ defect pair to ER configuration at E = a) 0, b) 0.25, c) 0.28. Then d) 0.28 , e) 0.21, and f) 0 V μm^{-1}. Scale bar corresponds to 15 μm.

V s^{-1} through the transition at approximately V = 2.2 V (corresponding to E = 0.28 V μm^{-1}), and then back to V = 0. As before, bright field images (no polarizers) were recorded for one ramping; transmission polarized optical microscopy images for the subsequent ramping. A series of bright field images is shown in Fig. 5, where we observed the following features:

15. The initially split defects (Fig. 5a) each presented as a line segment, which corresponded to the projection in the xy-plane of the disclination lines running between master and opposing surfaces.
16. On increasing the electric field (Figs. 5b and 5c) the line segments became shorter, indicating that the disclination lines were becoming more vertical. The spacing between the two defects also appeared to be decreasing with increasing field. We again note that the Joule heating due to the electric field was of order a few microwatts, thus having negligible impact on the results.
17. At no point did the defects appear to co-rotate, in contrast to the behaviour of the negative dielectric anisotropy liquid crystal.
18. Following a sudden transition, which occurred on a time scale faster than our ability to image the transition details, an ER configuration supplanted the defect pair. On decreasing the voltage to zero the width of the ER configuration decreased. This is seen in Figs. 5e and 5f, as well as in Fig. 6.
19. The ER configuration remained stable on returning to zero voltage, i.e., to E = 0.
20. Although this work focuses on positive strength defects, we also obtained videos of the m = -1/2 configuration (Supplementary Video 3). The apparent discontinuous behaviour of the transition at similar threshold fields occurred in this geometry as well.

The first point to note is that the observed behaviour could be viewed in first approximation as the ER to split defect video run in reverse (aside from the co-rotating line segments). For the same reasons discussed earlier, the pathway for a continuous transition does not seem to be the operative mechanism. Rather, the transition from split to ER occurred discontinuously, likely with melting of the core region. This may occur either just after the merger of the two half-integer defects into an m = +1 defect, or perhaps without the even temporary appearance of the integer defect.

Second, initially at V = 0 the director is expected to lie mostly in the *xy*-plane, except possibly for some small out-of-plane component just around the disclination line. We note that it *is* possible for the director to be entirely two-dimensional here, as recently demonstrated by Ferris, et al[10], but our conclusions do not require an absolute 2D director profile at V = 0. Nevertheless, as the voltage is increased, a *z*-component of the director may develop in the vicinity of the disclination lines, especially away from the master substrate. There are two consequences: i) The repulsive elastic force that tends to mutually repel the charged disclination lines is reduced, permitting the disclination lines to approach each other and thereby become less tilted and more vertical[25] (Figs. 5b and 5c, and compare with Fig. 1b), and ii) the half-integer defects become unstable because their topologically-protected 2D director field is being challenged by the electric field's propensity to drive the $\Delta\varepsilon > 0$ liquid crystal director along the *z*-axis. The result is that for sufficiently large field the m = +½ defect pair no longer is stable, the cores melt, merge, and then reappear as an ER configuration with positive director anisotropy.

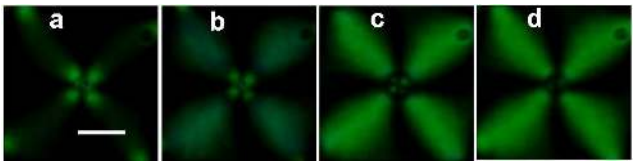

Fig. 6 Polarized optical microscope images using a green bandpass filter of the ER configuration in 5CB with decreasing field: a) E = 0.29, b) 0.28, c) 0.22, and d) 0 V μm^{-1}. Scale bar corresponds to 15 μm.

Figure 6 shows a sequence of polarized optical microscope images of the $\Delta\varepsilon > 0$ liquid crystal *after* conversion to the ER configuration and as the voltage was reduced back to zero (See also Electronic Supplementary Information, video 4). In these images the director was returning to the xy-plane far from the ER core, which means that the total optical retardation α was increasing over most of the region, except right at the core. This can be seen in the sequence of Figs. 6a through 6d. Generally, the transmitted light is minimum at two types of locations[9]: i) in regions where the director projection in the *xy*-plane is parallel or perpendicular to the polarizer, and ii) in regions where the optical retardation $\alpha = 2j\pi$, where j is an integer. Given the thickness h of the cell, this would correspond to $\alpha = 2\pi$ or 4π for the LC cell under consideration; the cell was insufficiently thick and the birefringence was insufficiently large for α to reach the next level of 6π. At the highest field shown (Fig. 6a) much of the image was dark, indicating that the retardation $\alpha = 4\pi$, as the $\alpha = 2\pi$ region was already close to the ER core where the director possessed a large z-component. As the electric field was reduced, in Figs. 6b through 6d, one sees a dark ring that corresponds to the $\alpha = 4\pi$ region moving closer to the ER core[9]. This is the key signature demonstrating the ER configuration, and is consistent with the director of a $\Delta\varepsilon > 0$ liquid crystal collapsing back toward the *xy*-plane, especially away from the core. At E = 0 the director in the region beyond the $\alpha = 4\pi$ dark ring resided mostly in the *xy*-plane (where $\alpha > 4\pi$), and the dark ring corresponded to the region in which the z-component of the director was sufficiently large to reduce the retardation α to 4π. Closer to the core the retardation continued to decrease with decreasing distance r from the core (as the *z*-component of the director increased), eventually reaching the $\alpha = 2\pi$ ring very close to the ER core. If the escape were complete, *i.e.*, if the director were parallel to the *z*-axis at the core, the optical retardation would reach zero at r = 0. If escape were only partial, as has been observed previously[9], the retardation would be finite at r = 0. We remark, however, that incomplete escape would mean that the core would be considered a topological defect rather than a true escaped radial configuration.

4 Numerical Results

Wishing to validate our experimental method, we chose to perform a numerical simulation of the ER to split defect transition. Our numerical procedure was based on a mesoscopic Landau-de Gennes model with a parametrized **Q** tensor, which is described in more detail in Appendix A, Section 6. Previously we have used this method successfully to simulate the electric field-driven "rewiring" of multistable nematic disclination lines, obtaining behaviours virtually identical to the experimental results.[26]

We minimised the free energy deep inside the nematic phase. At the top and bottom surface we enforced weak anchoring $w^{(i)}$ (Eq. 3c in the Appendix) of an isolated m = +1 defect patterned using Eq. 1 in the Appendix, and we used free boundary conditions at lateral walls. We note that we did not observe any transition from the escaped radial to split structure when running the simulations with infinitely strong anchoring conditions. Thus, the anchoring strength $w^{(i)}$ was reduced to a finite value, where the transition was observed. This immediately suggests that the experimental result, *viz.*, a discontinuous ER to split defect transition at a critical field E_{th}, depends critically on the choice of material parameters in the problem. For our calculations, we used the material parameters for Merck's ZLI-4330 specified by the manufacturer, the usual equal elastic constant approximation, as well as a typical value for anchoring, viz., $w^{(i)} = 10^{-5}\ \mathrm{Jm}^{-2}$.

We used the ER structure as the starting configuration and increased the applied field (Figs. 7a,b). The increasing electric field drove the director toward the xy-plane, except at the defect's core. At some threshold field $E = E_{th}$, the entire director profile, except for the defect core, continued to realign to become planar, *i.e.*, to lie in the xy-plane, with an m = +1 defect (Figs. 7c,d). In our calculations E_{th} was found to be ~ 20 V μm^{-1}. At this same field $E = E_{th}$ the director in the defect core underwent a slower realignment, which can be interpreted as melting of the core and conversion from positive to negative uniaxial symmetry. It is important to note that neither decomposition of the surface m = +1 defect nor formation of a disclination loop was observed for $E < E_{th}$, which would have been the case for the continuous transition pathway described in Section 1. Ultimately, with the topological protection due to the director's planar orientation, the m = +1 defect split into two m = +1/2 defects (Figs. 7e,f) spaced a few micrometers apart, consistent with the experimental results. The entire process occurred at the fixed electric field $E = E_{th}$ over a time scale of order 1 ms, which is sensitive to, among other parameters, the viscosity and is not inconsistent with the rapid transition observed experimentally. We note that this time scale was determined by using a time step based on the biaxial relaxation time. With the number of time steps needed to obtain a stable structure, we were able to determine the timescale.

In Appendix B we estimate the energy barriers among the competing structures using a uniaxial Frank-Oseen-type approach in terms of the nematic director field. Accordingly, the barriers are larger than $10^4\ k_B T$.

Thus, the numerical simulation was qualitatively consistent with the experimental observation and interpretation of a discontinuous transition. We note that co-rotation of the defects was not seen in our simulations even though E_{th} is well above the field at which the co-rotations were observed experimentally.

5 Conclusions

We examined an electric field-driven transition between two defect configurations: an m = +1 escaped radial and decomposed pair of half-integer defects. In principle, the transition between the two configurations can be along a continuous or discontinuous path. Experiments indicate that the transition likely is discontinuous, accompanied by a melting of the defect core at a characteristic threshold field. This melting is required by topology. Along the ER symmetry axis the nematic ordering is positive uniaxial. However, the cores of line defect comprising the split-defect structures are negatively uniaxial. For this reason the ER-split defect transition exhibits a transient melting event[27].

We argue that the discontinuous transition need not be the only pathway, as sufficiently strong planar anchoring may facilitate a continuous transition: splitting at the surface of an m = +1 escaped radial defect into a pair of m = +½ defects connected by a disclination loop at V = 0. But for our liquid crystal and (sufficiently weak) anchoring conditions, such continuous behaviour was observed neither experimentally nor by numerical simulations, and thus the ER to split transition was deemed first order. Our numerical simulation was found to be qualitatively consistent with the experimental result for the ER to split transition. Quantitative differences were due largely to the precise value of weak anchoring chosen for the numerical solution, as the actual experimental value was unknown.

Additionally, we note that in bulk a 3D point defect having a topological charge 1 is, according to recent experimental observations[28], expected to exhibit a small loop. This is consistent with numerical simulations[29], which reveal that this loop indeed consists of a torus exhibiting maximal biaxiality, which surrounds a ring displaying negative uniaxiality. However, our simulations reveal that the detailed structure of enforced $|m| = 1$ *surface* defects (boojums) depend on the surface anchoring strength. For strong enough anchoring, the boojum exhibits a loop-like structure. In this case, the ER-split defect transition is continuous on increasing E in LCs exhibiting a negative dielectric anisotropy. However, for sufficiently weak anchoring, which is the typical case experimentally, the boojum structure is qualitatively different and in this case, the transition is discontinuous. The detailed structure of boojums as a function of anchoring strength will be published elsewhere.

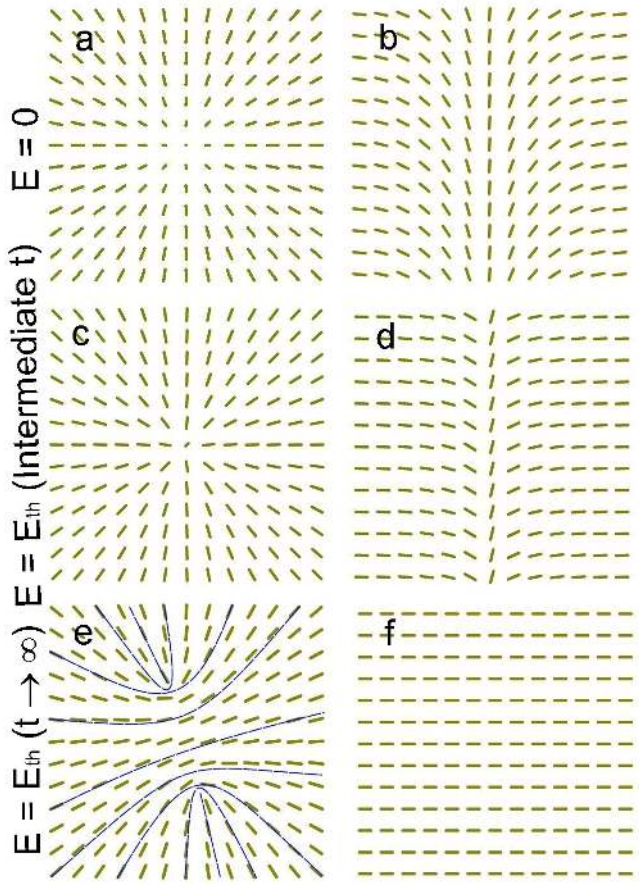

Fig. 7 Numerical results for director fields. a) $E = 0$, projection into xy-plane at $z = h/2$. b) $E = 0$, projection into the xz-plane at y = 0. c) $E = E_{th}$ at an intermediate time as the transition is occurring, projection into xy-plane at $z = h/2$. d) $E = E_{th}$ at an intermediate time as the transition is occurring, projection into xz-plane at $y = 0$. e) $E = E_{th}$, long after the transition has occurred, projection into xy-plane at $z = h/2$. Note the streamlines that highlight the pair of m = +1/2 defects. f) $E = E_{th}$, long after the transition has occurred, projection into xz-plane at y = 0.

An additional observation was the co-rotation of a pair of m = +½ defects for a negative dielectric constant liquid crystal at sufficiently high applied fields and low frequencies. The mechanism for this phenomenon currently is not understood, and will be pursued in future work.

6 Appendix A

i. Geometry of the problem

We use controlled boundary conditions, i.e., topology at the substrates, to stabilize TDs in the LC[17]. The bottom master and the top opposing planar-aligning substrates are located at $z = 0$ and $z = h$ respectively. The substrate was patterned for a topological defect of strength m = +1 (with zero phase, corresponding a radial director pattern) defined by the equation

$$\boldsymbol{\varphi(x,y) = \arctan\left(\frac{y-y_d}{x-x_d}\right) + \varphi_0} \qquad (1)$$

This is the solution to Laplace's equation in the equal elastic constant approximation[30]. Here φ corresponds to the azimuthal orientation of the nematic director with respect to the x-axis and x_d and y_d correspond to the x and y location of the defect core on the substrate. Furthermore, we apply a spatially homogeneous electric field E along the z-axis and consider LCs with negative dielectric anisotropy[31]. Finally, we used a 100x100x100 mesh and chose the scale to match with the experiments, so that we could compare the results directly.

ii. Modelling

We used a mesoscopic Landau-de Gennes approach[31] in which nematic orientational order is modelled by the traceless, symmetric tensor nematic order parameter $\boldsymbol{Q} = \sum_{i=1}^{3} \lambda_i(\boldsymbol{e}_i \otimes \boldsymbol{e}_i)$, $\boldsymbol{e}_i$ are the eigenvectors and λ_i the corresponding eigenvalues in the Cartesian (x,y,z) coordinate system. We considered LCs that exhibit equilibrium nematic uniaxial order, generally given[31] as $\boldsymbol{Q}^{(u)} = S\left(\boldsymbol{n} \otimes \boldsymbol{n} - \frac{1}{3}\boldsymbol{I}\right)$. Here $S \in [-1/2,1]$ is the uniaxial order parameter, the unit vector field $\boldsymbol{n}$ is the nematic director field, and $\boldsymbol{I}$ is the unit tensor.

We assume that the evolution in space and time of the nematic order is determined by[32] $\gamma\, d\boldsymbol{Q}/dt = -\delta F/\delta \boldsymbol{Q}$, where the LC's lossy properties can be described by the single material parameter γ. The free energy is

$$\boldsymbol{F} = \int (\boldsymbol{f_c} + \boldsymbol{f_e} + \boldsymbol{f_f})\boldsymbol{d^3r} + \sum_{\boldsymbol{i}} \int \boldsymbol{f_s^{(i)}} \boldsymbol{d^2r} \qquad (2)$$

This corresponds to a volume integral over the nematic cell for the condensation (f_c), elastic (f_e), and external field (f_f) contributions, and the sum of integrals over all the interfaces for the surface $\left(f_s^{(i)}\right)$ contribution. These terms correspond individually to[31]

$$\boldsymbol{f_c} = \frac{\boldsymbol{1}}{\boldsymbol{2}}\boldsymbol{A_0}(\boldsymbol{T} - \boldsymbol{T^*})\boldsymbol{TrQ^2} - \frac{\boldsymbol{1}}{\boldsymbol{3}}\boldsymbol{B}\,\boldsymbol{TrQ^3} + \frac{\boldsymbol{1}}{\boldsymbol{4}}\boldsymbol{C}\left(\boldsymbol{TrQ^2}\right)^2, \qquad (3a)$$

$$\boldsymbol{f_e} = \frac{\boldsymbol{1}}{\boldsymbol{2}}\boldsymbol{L}|\boldsymbol{\nabla Q}|^2, \qquad (3b)$$

$$\boldsymbol{f_s^{(i)}} = \frac{\boldsymbol{w^{(i)}}}{\boldsymbol{2}}\boldsymbol{Tr}\left(\boldsymbol{Q} - \boldsymbol{Q_s^{(i)}}\right)^2, \qquad (3c)$$

$$\boldsymbol{f_f} = -\frac{\mathbf{1}}{\mathbf{2}}\boldsymbol{\varepsilon_0 \Delta\varepsilon E^2\, e_E \cdot Q e_E}\,. \qquad (\mathbf{3}\boldsymbol{d})$$

Here A_0, B, C are material parameters, T^* is the supercooling temperature of the isotropic phase, L is a representative characteristic elastic modulus in the single elastic constant approximation, the anchoring coefficient $\boldsymbol{w^{(i)}}$ describes the strength of the preferred surface orientation at the i-th surface given by $\boldsymbol{Q_s^{(i)}}$, where $\boldsymbol{w^{(i)} \to \infty}$ corresponds to the strong anchoring limit, $\boldsymbol{E = Ee_E}$ is the external electric field pointing along the unit vector $\boldsymbol{e_E}$, $\boldsymbol{\varepsilon_0}$ is the permittivity of free space, and $\boldsymbol{\Delta\varepsilon}$ is the anisotropy of the dielectric constant.

We use the parametrisation for $\boldsymbol{Q}$ in Cartesian coordinates defined by the unit vectors $(\boldsymbol{e_x}, \boldsymbol{e_y}, \boldsymbol{e_z})$:

$$\boldsymbol{Q} = \begin{bmatrix} \boldsymbol{q_1 + q_2} & \boldsymbol{q_3} & \boldsymbol{q_4} \\ \boldsymbol{q_3} & \boldsymbol{q_1 - q_2} & \boldsymbol{q_5} \\ \boldsymbol{q_4} & \boldsymbol{q_5} & \boldsymbol{-2q_1} \end{bmatrix}, \qquad (\mathbf{4})$$

where q_1, q_2, q_3, q_4, and q_5 are variational parameters.

For scaling purposes we introduce[31] the dimensionless temperature $r = (T - T^*)/(T^{**} - T^*)$ and the scaled order parameter $\boldsymbol{Q} = \boldsymbol{Q}/S_0$, where $S_0 = B/4C$ and $T^{**} = T^* + B^2/(24A_0C)$ is the superheating temperature associated with the (weakly) first order phase transition. We scale distances with respect to h, and the time is measured with respect to the characteristic order parameter relaxation time $\tau = 2\gamma/[3A_0(T^{**} - T^*)]$ expressed at $T = T^{**}$.

The resulting dimensionless free energy densities $\tilde{f}_c$, $\tilde{f}_e$, and $\tilde{f}_f$ are

$$\tilde{\boldsymbol{f}}_{\boldsymbol{c}} = \frac{\boldsymbol{r}}{\mathbf{6}}\boldsymbol{TrQ^2} - \frac{\mathbf{2}}{\mathbf{3}}\boldsymbol{Q^3} + \frac{\mathbf{1}}{\mathbf{8}}\left(\boldsymbol{Q^2}\right)^2, \qquad (\mathbf{5a})$$

$$\tilde{\boldsymbol{f}}_{\boldsymbol{e}} = \left(\frac{\boldsymbol{\xi_b}}{\boldsymbol{h}}\right)^2 \left|\tilde{\boldsymbol{\nabla}}\boldsymbol{Q}\right|^2, \qquad (\mathbf{5}\boldsymbol{b})$$

$$\tilde{\boldsymbol{f}}_{\boldsymbol{s}} = \frac{\boldsymbol{\xi_b^2}}{\boldsymbol{d_e h}}\ \boldsymbol{Tr}\left(\boldsymbol{Q} - \boldsymbol{Q_s^{(i)}}\right)^2 \qquad (\mathbf{5}\boldsymbol{c})$$

$$\tilde{\boldsymbol{f}}_{\boldsymbol{f}} = -\left(\frac{\boldsymbol{\xi_b}}{\boldsymbol{\xi_E}}\right)^2 \boldsymbol{e_E \cdot Q e_E} \qquad (\mathbf{5}\boldsymbol{d})$$

Here $\xi_b = 2\sqrt{LC}/B$ is the bare biaxial correlation length[32], $d_e = L/w^{(i)}$ is the surface extrapolation length, $\xi_E = \sqrt{LS_0/(\varepsilon_0\Delta\varepsilon E^2)}$ is the external field extrapolation length[31,33] expressed at the superheating temperature, and $\tilde{\nabla} = h\nabla$.

7 Appendix B

To estimate the energy barrier separating the *escaped radial* (ER) and *split defect* (SD) configuration we use the results derived by Chiccoli *et al*[11]. They used the uniaxial Frank-Oseen-type description in the one-constant approximation, where nematic structures are determined solely by the nematic director field $\boldsymbol{n}$. We consider the ER-SD transformation pathway, which was realized in our experimentally observed electrical field E driven ER-SD transformation in a nematic LC exhibiting the negative dielectric anisotropy. In this transition, on increasing E the initial ER-type nematic director was increasingly confined to the (x,y) planes within the cell. At the critical field E_{th}, the structure exhibiting a single m=+1 disclination line was (at least temporarily) formed, to which we refer as the *single line defect* (SLD) structure. This configuration split into two m=+1/2 line defects, forming the SD configuration and remained metastable when E was switched off. In this scenario, the SLD structure corresponds to the most energetic intermediate configuration. Therefore, the free energy differences $\Delta F_1 = F^{(SLD)} - F^{(ER)}$ and $\Delta F_2 = F^{(SLD)} - F^{(SD)}$ well estimate the energy barriers among the competing structures. We first estimate the barriers in the absence of E. In the second step we include in the estimate the external electric field free energy contribution and discuss the impact of the cell thickness h on the threshold value E_{th}.

i. Energy barrier

In the absence of E the dimensionless excess free energies $\Delta\tilde{F}^{(str)} = (F^{(str)} - F_c)/(\pi Kh)$ of the structures are[11]

$$\Delta\tilde{F}^{(SLD)} \sim \ln\left(\frac{R}{r_1}\right) + u_1, \qquad (6a)$$

$$\Delta\tilde{F}^{(SD)} \sim \frac{1}{2}\ln\left(\frac{2R^2}{r_{1/2}\,\Delta r}\right) + 2u_{1/2}, \qquad (6b)$$

$$\Delta\tilde{F}^{(ER)} \sim \ln\left(\frac{R}{d}\right) + g. \qquad (6c)$$

Here $F^{(str)}$ stands for the free energy of a structure, viz., SLD, ER, or SD, and F_c stands for the equilibrium nematic free energy condensation penalty. The structures are considered within a cylindrical domain of radius R within a plane-parallel cell. The domain's cylindrical axis is set perpendicular to the point where the m=1 surface defect is imposed by the bottom confining substrate. Furthermore, u_1 and $u_{1/2}$ are dimensionless core energies, and r_1 and $r_{1/2}$ estimate the defect core radii of m=+1 and m=+1/2 disclinations, respectively. The characteristic separation distance of m=+1/2 defects in the SD structure equals to Δr, g is a constant, $K \sim LS_{eq}^2$ stands for the representative Frank elastic constants, and S_{eq} is the equilibrium nematic uniaxial order parameter.

For the condition of interest it holds that $u_1 \sim u_{1/2} \sim 1$, $r_1 \sim r_{1/2} \sim \xi_b$, and $g \sim 4.1$ (see Ref. 11). In Fig. 8 we plot the competing free energy densities as a function of the cell thickness h, where we set $\xi_b = 10$ nm, $\Delta r = 3\ \mu m$, $R = 10\ \mu m$. For this set of parameters ER corresponds to global minimum for $h > 1\ \mu m$. For $K = 5\ 10^{-12}$ J and h=8 μm we obtain energy barrier estimates $\Delta F_1 \sim 3.6\ 10^4\ k_BT$ and $\Delta F_2 \sim 2.1\ \ 10^4\ k_BT$,

respectively, where k_B stands for the Boltzmann constant and $T \sim 300$ K.

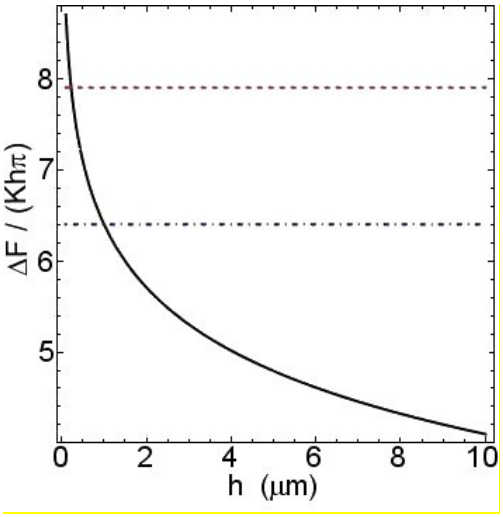

Fig. 8 Excess free energy penalties $\Delta F = \pi K h\, \Delta\tilde{F}$ of the ER (solid line), SD (dash-dotted line), and SLD (dashed line) as a function of cell thickness.

II. Electrical threshold field

We next estimate the threshold field E_{th} triggering the ER-SD transition, where for E=0 the ER structure is stable and the LC possesses a negative dielectric anisotropy. In the free energy estimates given by Eqs. 6 we add the external field free energy contribution, see Eq. 3d, where $\boldsymbol{E} = E\boldsymbol{e}_z$. Note that this contribution equals zero for the SD structure in which $\boldsymbol{n}$ is planar, and consequently $\boldsymbol{n}.\boldsymbol{E} = 0$. However, the field affects the ER structure, for which

$$\Delta\tilde{F}^{(ER)} \sim \ln\left(\frac{R}{d}\right) + g + \left(\frac{R}{\xi_E}\right)^2 \langle(\boldsymbol{n}.\boldsymbol{e}_z)^2\rangle. \quad (7)$$

Here $\langle(\boldsymbol{n}.\boldsymbol{e}_z)^2\rangle$ stands for the spatial average of $(\boldsymbol{n}.\boldsymbol{e}_z)^2$ within the cylindrical domain. The threshold field is determined from the condition $\Delta\tilde{F}^{(ER)} - \Delta\tilde{F}^{(SD)} = 0$, from which it follows

$$\frac{R}{\xi_E^{(th)}} \sim \sqrt{\left(\frac{1}{2}\ln\left(\frac{2R^2}{r_{1/2}\,\Delta r}\right) + 2u_{1/2} - \ln\left(\frac{R}{d}\right) - g\right) / \langle(\boldsymbol{n}.\boldsymbol{e}_z)^2\rangle}. \quad (8)$$

Here $\xi_E^{(th)}$ marks the critical value of ξ_E. The estimate suggests that E_{th} depends relatively weakly on h. Note that this ansatz works relatively badly for a quantitative analysis. For example, using typical material and geometric parameters, mimicking our samples, and setting $E_{th} \sim 30$ V/μm as our experiment suggest, Eq. 8 would be fulfilled for $\langle(\boldsymbol{n}.\boldsymbol{e}_z)^2\rangle \sim 0.001$. However, typical ER profiles[11] yield $\langle(\boldsymbol{n}.\boldsymbol{e}_z)^2\rangle \sim 0.02$. The reason for this discrepancy is a relatively strongly deformed director field at the threshold condition, which is not taken into account in Eq. 7. Note that this effect is well visible in our simulations, see Fig. 7d.

Conflicts of interest

There are no conflicts to declare.

Acknowledgments

We thank Profs. Zvonimir Dogic and Hillel Aharoni for valuable communications. This work was supported by the National Science Foundation under grants DMR1505389 and DMR1901797 and by the National Aeronautics and Space Administration under grant NNX17AC76G and the Slovenian Research Agency (ARRS) under contracts P1-0099 and PR-07585.

Notes and references

1 N. Mermin, *Rev. Mod. Phys.*, 1979, **51**, 591
2 W. H. Zurek, *Nature* 1985, **317**, 505
3 Y. Zhenwei and M.O. Cruz, *Proc. Nat. Acad. Sci.*, 2014, **111**, 5049
4 T.W.B. Kibble, *J. Phys. A Math Gen.*, 1976, **9**, 1387
5 A. Martinez, M. Ravnik, B. Lucerno, R. Visvanathan, S. Žumer, and I.I. Smaylyukh, *Nature Mater.*, 2014, **13**, 258
6 M. Kleman and O.D. Lavrentovich, **Soft Matter Physics**, Springer-Verlag, New York 2003
7 F. Serra, *Liq. Cryst.*, 2016, **43**, 1920
8 S. Zhou, S.V. Shiyanovskii, H.-S. Park, and O.D. Lavrentovich, *Nature Comm.*, 2017, **8**, 14974 (DOI: 10.1038/ncomms14974)
9 B.S. Murray, S. Kralj, and C. Rosenblatt, *Soft Matter*, 2017, **13**, 8442
10 A.J. Ferris, S. Afghah, R.L.B. Selinger, J.V. Selinger, and C. Rosenblatt, *Soft Matter*, 2020, **16,** 642
11 C. Chiccoli, I. Feruli, O. D. Lavrentovich, P. Pasini, S. V. Shiyanovskii and C. Zannoni, *Phys. Rev. E: Stat., Nonlinear, Soft Matter Phys.*, 2002, **66**, 030701
12 G. Carbone, G. Lombardo, R. Barberi, I. Musevic, and U. Tkalec, *Phys. Rev. Lett.*, 2009, **103**, 167801
13 Ph. Martinot-Lagarde, H. Dreyfus-Lambez, and I. Dozov, *Phys. Rev. E,* 2003, **67**, 051710
14 R.J. Ondris-Crawford, G.P. Crawford, S. Zumer, and J.W. Doane, *Phys. Rev. Lett.*, 1993, **70**, 194
15 I.I. Smalyukh, R. Pratibha, N.V. Madhusudana, and O.D. Lavrentovich, *Eur. Phys. J. E*, 2005, **16**, 179
16 P. E. Cladis and M. Kleman, *J. Phys.*, 1979, **40**, 325.
17 B. S. Murray, R. A. Pelcovits and C. Rosenblatt, *Phys. Rev. E: Stat., Nonlinear, Soft Matter Phys*., 2014, **90**, 052501
18 J.L. Ericksen, **Liquid Crystals and Ordered Fluids** (ed. J. Johnson and R.S. Porter, Plenum, New York, 1970
19 A. S. Backer, A. C. Callan-Jones, and R. A. Pelcovits, *Phys. Rev. E* 2008, **77**, 021701
20 A. Bricard, J.-B. Caussin, N. Desreumaux, O. Dauchot, and D. Bartolo, *Nature*, 2013, **503**, 95
21 M.M. Norton, A. Baskaran, A. Opathalage, B. Langeslay, S. Fraden, A. Baskaran, and M.F. Hagan, *Phys. Rev. E*, 2018, **97**, 012702
22 A.K. Bhattacharjee, *Scientific Rep.*, 2018, **8**, 2517
23 W. Helfrich, *J. Chem. Phys.*, 1969, **51**, 4092
24 P. Oswald and A. Dequidt, *Liq.Cryst.* 2009, **36**, 1071
25 S. Afghah, R.L.B. Selinger, and J.V. Selinger, *Liq. Cryst.*, 2018, **45**, 2022
26 S. Harkai, B.S. Murray, C. Rosenblatt, and S. Kralj, *Phys. Rev. Research* 2020, **2**, 013176
27 S. Kralj, R. Rosso, and E.G. Virga, *Phys. Rev. E*, 2010, **81**, 021702

28 X. Wang, Y.-K. Kim, E. Bukusoglu, B. Zhang, D.S. Miller, and N.L. Abbott, *Phys. Rev. Lett.* 2016, **116,** 147801
29 S. Kralj, E.G. Virga, and S. Žumer, *Phys. Rev. E* 1999, **60**, 1858
30 J. Nehring and M. Saupe, *J. Chem. Soc., Faraday Trans. 2,* 1972, **68**, 1
31 P.G. DeGennes and J. Prost, **The Physics of Liquid Crystals**, Clarendon, Oxford, 1972
32 M. Ravnik and S. Žumer, *Liq. Cryst.,* 2009 **36**, 1201
33 F. Bisi, E. C., Garland, R. Rosso, and E. G. Virga, *Phys. Rev. E* 2003**, 68**, 021707